ROSE bitumen: Mesoscopic model of bitumen and bituminous mixtures

Claire A. Lemarchand,[1,2] Michael L. Greenfield,[3] Jeppe C. Dyre,[2] and J. S. Hansen[2,a)]
[1]CEA, DAM, DIF, 91297 Arpajon Cedex, France
[2]"Glass and Time," IMFUFA, Department of Science and Environment, Roskilde University, P.O. Box 260, DK-4000 Roskilde, Denmark
[3]Department of Chemical Engineering, University of Rhode Island, Kingston, Rhode Island 02881, USA

We present a mesoscopic model for bitumen and bituminous mixtures. The model, which is based on dissipative particle dynamics, consists of different dynamical entities that represent the different characteristic time scales. Through the stress relaxation function, the mechanical properties of the model are investigated. For pure bitumen, the viscosity features super-Arrhenius behavior in the low-temperature regime in agreement with experimental data. The frequency-dependent viscoelastic properties show purely viscous behavior at low frequencies with increasing elasticity and hardening at higher frequencies, as expected. The model dynamics are analyzed in the framework of longitudinal hydrodynamics. The thermal process is two orders of magnitude slower than the attenuation of the density-wave propagation; hence the dynamic structure factor is dominated by a sharp Rayleigh peak and a relatively broad Brillouin peak. The model is applied to study triblock-copolymer-modified bitumen mixtures. Effects of the polymer concentration and end-block interactions with the bitumen are investigated. While the polymer concentration has an effect on the mechanical properties, the effect of increasing repulsive interactions between the bitumen and the polymer end-blocks is much more dramatic; it increases the viscosity of the mixture and shifts the onset of the elastic behavior to lower frequencies. For increased repulsion, the polymer end-blocks form small clusters that can be connected by a dynamic polymer backbone network. A simple Flory-Huggins analysis reveals the onset of segregation of the end-blocks in the bitumen mixture in agreement with the simulation data. Hence the changed mechanical properties are due to the emergence of large-scale structures as the repulsion is increased, which conforms to known mechanisms of microphase separation in polymer-modified bitumens. *Published by AIP Publishing.* https://doi.org/10.1063/1.5047461

I. INTRODUCTION

Bitumen is a product of oil refinery processes, and its primarily role is as the binding material in road pavement. Because bitumen is a residue product, its chemical composition is not unique; it is composed, primarily, of saturated, naphthenic, and aromatic hydrocarbons with molecular masses above 200 g/mol.[1–3] Heteroatoms, like sulfur, are also present and are believed to play a role in the chemical aging of bitumen although other mechanisms may also be relevant.[4] The road deterioration processes and durability are partly due to the changing mechanical properties of the bitumen binder;[4] however, the properties can be modified by mixing polymers with bitumen[5] such that pavement resistance to road rutting, fatigue cracking, and moisture resistance increases. Polymer modified bitumens (PMBs) are very complex multiphase mixtures, and the design of new road pavement materials calls for a fundamental understanding of these systems rather than only relying on trial-and-error experiments.

In recent years, detailed molecular dynamics simulations have been undertaken to study bitumen[6–12] and have resulted in different molecular bitumen models by our groups.[11,13,14]

For example, the Cooee-bitumen model is a united-atom-unit model based on four characteristic molecules. Common for these investigations are the limited characteristic time scales on the order of 1 to 10 ns using standard central processor unit computers[7] and to a few microseconds using coarse graining and graphic-card based computations.[14,15] Therefore, only fast and usually single molecular processes can be investigated. The collective processes that determine the mechanical properties are associated with a large noise-to-signal ratio and may therefore only be estimated from models,[7,12] evaluated directly at sufficiently high temperatures,[14,16] evaluated at lower temperatures with noise reduction methods,[17,18] or evaluated through non-equilibrium simulations in the non-Newtonian regime.[19] The challenge becomes even more evident for PMBs, in which the system characteristic time and length scales increase dramatically. Here only bitumen and part of a single homopolymer[20] or a random copolymer[16] chain, each within a single phase, have been simulated with detailed simulations. Finally, molecular-scale time-temperature superposition (TTS) has been demonstrated recently.[21]

One important result from molecular dynamics is that there exist several molecular time scales. For example, the diffusive time scale (molecular translational motion) for asphaltenes is quite long compared to the time scale for the

---

a)jschmidt@ruc.dk

saturate component. This slow diffusivity is due to the formation of asphaltene aggregates with large masses and slower translational motion.[9,20] Also, molecular rotational motion and end-to-end relaxations introduce different time scales.[8,12,14] Coupling among these time scales results in collective properties of interest, like viscosity, when designing new binder materials for road pavement.

To address the problem of reaching the necessary time scale, we propose here a new bitumen model. The model is coarse grained in the sense that it excludes molecular and atomic details, yet it includes many different dynamical time scales. The model is generic in that it can represent any complex system characterized by different time scales. Like real bitumen, the model is not unique and one may vary the model components in accordance with bitumen age, oil origin, and so forth. With such a high degree of coarse graining, the model predictions are only qualitative; however, it allows for the investigation of modified bituminous mixtures. It expands on a related study by our group on the mechanics experienced by different coarse-grained entities using dissipative particle dynamics (DPD).[22] The model is called "ROSE bitumen" as the aim of the model is to bring new insight into the mechanical properties of road pavements designed under the ROads Saving Energy (ROSE) program.

The Superpave guidelines[23] proposed that pavement designs are based on the magnitude of the dynamic modulus, $|G^*|$, and phase angle, δ. To prevent rutting, the loss compliance must be sufficiently small and thus $|G^*|/\sin(\delta)$ must be sufficiently large; that is, the pavement must be difficult to deform and any deformation should mainly be elastic. Cracking resistance requires a deformable elastic material. We will not discuss these guidelines; however, we use G^* and δ to investigate the mechanical properties of the model. In the analysis, we also investigate the hydrodynamics. This shows that the thermal processes and density wave dampening occur on two different time scales. From this, we predict the characteristics of the dynamic structure factor of bitumen.

II. THE ROSE MODEL AND METHODOLOGY

The model is an ensemble of interacting spherical particles. The particles may be connected to form a molecule, by which we mean a dynamic component or entity that represents one or more single-particle dynamical time scales. See Fig. 1. Here we include three types of molecules—a dimer, pentamer, and cyclo-butamer—that represent (i) relatively fast and slow translational motion of the smaller saturates and aggregates, (ii) the slow rotational relaxations of the asphaltenes, and (iii) the different end-to-end relaxations. We shall use the terms "monomer" and "particle" interchangeably throughout the text. As noted above, the choice of molecules is not unique. The effect on the dynamics of adding polymers is modeled by linear entities composed of 20 monomers. Among the 20 monomers, the central 12 have the same interaction parameters as those of bitumen, while the four at each end may have different parameters. We label the end monomers in the polymer "S" and the polymer backbone
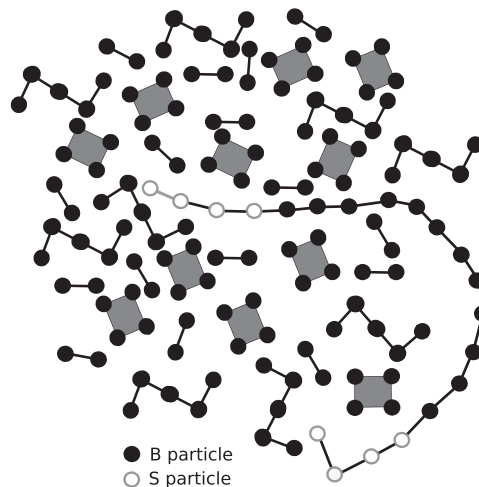

FIG. 1. Schematic illustration of the model. The bitumen is composed of three different molecule types representing different characteristic dynamics: (i) dimer, (ii) pentamer, and (iii) cyclo-butamer. Addition of a triblock copolymer is illustrated with two different monomers, S and B. The model is simulated in three dimensions.

and bitumen monomers "B," motivated by styrene-butadiene block copolymers in which the butadiene domain and bitumen are mutually compatible.[24,25] This distinction allows for the creation of polymer ends interacting more favorably with each other than with bitumen, potentially creating a network through the system, which is recognized experimentally as an important contribution of polymer modification to bitumen properties.[24]

The interactions are based on the dissipative particle dynamics (DPD) method.[26–28] Each monomer is a DPD particle with position, $\mathbf{r}_i$, and momentum, $\mathbf{p}_i$. The DPD particle dynamics follow Newton's equation of motion, $\mathbf{F}_i = m_i\ddot{\mathbf{r}}_i$, where m_i is the particle mass and $\mathbf{F}_i$ is the total force acting on particle i. In DPD, the force is a sum of three contributions: the conservative force, $\mathbf{F}_i^C$, the random force, $\mathbf{F}_i^R$, and the dissipative force, $\mathbf{F}_i^D$, i.e., $\mathbf{F}_i = \mathbf{F}_i^C + \mathbf{F}_i^R + \mathbf{F}_i^D$. The conservative force can be written in terms of the potential energy function of the system $\mathbf{F}_i^C = -\nabla_{\mathbf{r}_i} U(\mathbf{r})$, where $\mathbf{r} = (\mathbf{r}_1, \mathbf{r}_2, \ldots)$ and

$$
U(\mathbf{r}) = \frac{1}{2} \sum_i \sum_{j>i} a_{ij}\left(1 - \frac{r_{ij}}{r_c}\right)^2 + \frac{k_s}{2} \sum_{\text{bonds}} \left(\frac{r_{ij}}{l_b} - 1\right)^2 \\
+ \frac{k_\theta}{2} \sum_{\text{angles}} [\cos(\theta) - \cos(\pi/2)]^2 + k_\phi \sum_{\text{dihed.}} \cos(\phi).
$$

(1)

Here, a_{ij} are the interaction parameters that quantify the repulsion between particles i and j (depending on their type); $r_{ij} = |\mathbf{r}_{ij}|$, where $\mathbf{r}_{ij}$ is the vector of separation, $\mathbf{r}_{ij} = \mathbf{r}_i - \mathbf{r}_j$; r_c is the cut-off radius; l_b is the zero-force bond length; k_s, k_θ, and k_ϕ are constants; and θ and ϕ are the bond and dihedral angles, respectively. The first term on the right-hand side is due to nonbonded repulsive interactions and only applies when $r_{ij} < r_c$. The repulsion parameter value depends on whether the interaction takes place between two B particles, an S particle and a B particle or two S particles. The last two contributions are included for the case of cyclo-butamer in order to ensure that

the molecule is sufficiently planar. The random and dissipative forces are given by[28]

$$\mathbf{F}_{ij}^R = \frac{\sigma w(r_{ij})\zeta_{ij}}{\sqrt{\Delta t}}\hat{\mathbf{r}}_{ij} \;\; \text{and} \;\; \mathbf{F}_{ij}^D = -\frac{(\sigma w(r_{ij}))^2}{2mT}\left[\hat{\mathbf{r}}_{ij}\cdot(\mathbf{v}_i-\mathbf{v}_j)\right]\hat{\mathbf{r}}_{ij},$$
(2)

where σ is the random force amplitude, ζ_{ij} is a uniformly distributed random number with zero mean and unit variance, $\mathbf{v}_i$ is the velocity of particle i, Δt is the time step used in the integrator, and $w(r_{ij})$ is a weighing function. We use here the function suggested by Groot and Warren,[28] $w(r_{ij}) = r_c - r_{ij}$. We express any physical quantity and constants in reduced units as is common practice; see, e.g., Ref. 29. In all simulations, the amplitude is $\sigma = 3.0$, the time step $\Delta t = 0.01$, the spring constants $k_s = k_\theta = k_\phi = 25$, and the length $r_c = l_b = 1$. The repulsion parameters for two interacting particles of the same type are set to $a_{BB} = a_{SS} = 25$, while it varies for unlike types. The equations of motion are integrated using the standard velocity Verlet algorithm.[28] It is important to stress that the choices of parameters are not unique but are chosen in order to keep the simulations numerically stable for the time step chosen, to maintain sufficiently rigid molecules, to ensure proper thermostating, etc.

The bitumen composition is a mixture of 200 dimers, 200 pentamers, and 200 cyclobutamers. Hence the size of the system simulated is from 2200 to 2400 DPD particles, depending on the polymer concentration. The density is $\rho = 4.0$, and temperatures in the range $0.08 \leq T \leq 1.0$ have been simulated. For each temperature, five independent simulation runs were performed; the last four runs used the final configuration of the previous simulation. This allows us to investigate the system's equilibration process. In the first simulation, the molecular centers-of-mass are positioned on a simple lattice corresponding to the given mass density, and the DPD particles are given a random initial velocity corresponding to the given temperature. Each run is 5×10^6 time steps, that is, a total of 25×10^6 time steps. The simulations were carried out using the seplib molecular dynamics library.[30]

To investigate the mechanical properties of the model, we evaluate the molecular stress tensor $\boldsymbol{\sigma}$ from the Irving-Kirkwood definition[31]

$$V\boldsymbol{\sigma}(t) = -\sum_i \frac{\mathbf{P}_i\mathbf{P}_i}{M_i} - \sum_i\sum_{j>i}(\mathbf{R}_{ij}\mathbf{F}_{ij}^M)^T,$$
(3)

where V is the system volume, $\mathbf{P}_i$ is the total momentum of molecule i, M_i is the molecular mass, $\mathbf{R}_{ij}$ is the vector of separation of molecule i and j, and $\mathbf{F}_{ij}^M$ is the total force acting on i due to j; that is, $\mathbf{F}_{ij}^M = \sum_{\alpha\in i}\sum_{\beta\in j}\mathbf{F}_{\alpha\beta}$, where particle α is in molecule i and β is in molecule j. Note that capital letters denote molecular quantities. This definition of the stress does not include the dissipative and random force contributions. It has been pointed out that these forces should, in fact, be included;[32–34] however, recently Hansen *et al.*[35] noted that the viscosity evaluated from the Green-Kubo integral of the stress autocorrelation where definition (3) is used gives the correct hydrodynamic relaxation times.

In general, the molecular stress tensor is not symmetric,[36] and to calculate the viscosity, the traceless symmetric part is extracted from the definition $\overset{os}{\boldsymbol{\sigma}} = \frac{1}{2}(\boldsymbol{\sigma}+\boldsymbol{\sigma}^T) - \frac{1}{3}\text{trace}(\boldsymbol{\sigma})$. The complex shear viscosity is then found from the Fourier-Laplace transform[37]

$$\eta^*(\omega) = \frac{V}{k_BT}\int_0^\infty C(t)\,e^{-i\omega t}\,dt,$$
(4)

where $C(t)$ is the stress autocorrelation function

$$C(t) = \frac{1}{3}\sum_{nm}\langle\overset{os}{\sigma}_{nm}(t)\,\overset{os}{\sigma}_{nm}(0)\rangle.$$
(5)

The double index nm runs over the xy, xz, and yz components of the symmetric traceless stress tensor. From the complex viscosity, we have the frequency-dependent dynamic modulus $G^*(\omega) = G'(\omega) + iG''(\omega) = i\omega\eta^*(\omega)$ and the phase angle $\delta = \tan^{-1}(G''(\omega)/G'(\omega))$.

The viscosity characterizes the transverse dynamical properties of the bitumen. For completeness, we also include an investigation into the longitudinal dynamical properties of the model via the longitudinal velocity autocorrelation function, C_{uu}, and density autocorrelation function, $C_{\rho\rho}$. They are defined by[35,37]

$$C_{uu}(k,t) = \frac{1}{V}\langle\widetilde{u}_y(k,t)\widetilde{u}_y(-k,0)\rangle$$
(6)

and

$$C_{\rho\rho}(k,t) = \frac{1}{V}\langle\widetilde{\rho}(k,t)\widetilde{\rho}(-k,0)\rangle,$$
(7)

where k is the longitudinal component in the wavevector $\mathbf{k} = (0, k, 0)$ and $\widetilde{u}_y$ and $\widetilde{\rho}$ are the longitudinal velocity component and density in Fourier space defined from the molecular center-of-mass quantities as[35]

$$\widetilde{\rho}(k,t) = \sum_i M_i e^{-ikR_{i,y}(t)},$$
(8)

$$\widetilde{u}_y(k,t) = \frac{1}{\rho}\sum_i M_i V_{i,y}(t)e^{-ikR_{i,y}(t)},$$
(9)

where $R_{i,y}$ and $V_{i,y}$ are the longitudinal components of center-of-mass position and velocity of molecule i.

III. RESULTS

A. Mechanical properties

We start by discussing the mechanical properties of the pure bitumen model, i.e., without polymer additives. The zero-frequency shear viscosity, η_0, is first evaluated as a function of temperature from Eq. (4) using that $\lim_{\omega\to 0}\eta^* = \eta_0$. The results are shown in Fig. 2. It is seen that the viscosity follows a super-Arrhenius behavior for temperatures $T < 0.1$, whereas for higher temperatures, the behavior is Arrhenius. Real bitumens are super-Arrhenius over a large temperature range, particularly at lower temperatures, see, e.g., Refs. 14, 38, and 39, and we will therefore mainly focus on the temperature regime $0.1 \leq T \leq 0.2$ that includes the onset of the non-Arrhenius regime.

In Fig. 3(a), the normalized stress autocorrelation function, $C^N(t) = C(t)/C(0)$, is shown for $T = 0.2$ (open circles) and
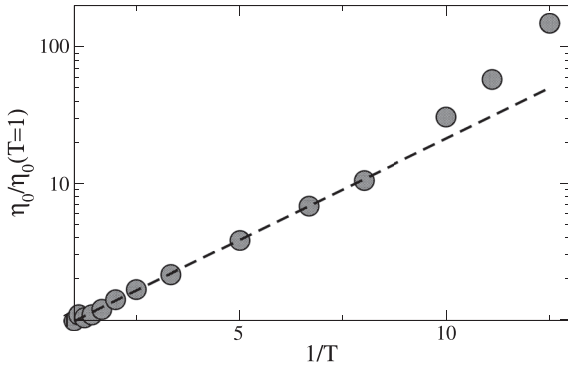
FIG. 2. Viscosity for the pure bitumen model as a function of inverse temperature. The line is a fit to data points for $0.3 \leq T \leq 1.0$, indicating the Arrhenius regime. Standard deviations are of the same magnitude as the size of the symbols.

$T = 0.1$ (open triangles). Note that the statistical uncertainty is represented by the standard error of the sample distribution, which is of the same magnitude as the symbol sizes. The stress relaxation features a fast decay followed by a slower decay. We interpret the fast decay as the collective molecular center-of-mass vibrations, i.e., the oscillatory system phonon mode. The oscillatory behavior is observed clearly at high temperatures, but it is not visible in the relaxation function for $T < 0.1$, even though the phonon mode must still be present. We assign the slow decay in the relaxation function to structural collective rearrangements in the system.

Inspired by Badami and Greenfield[40] and Hartkamp *et al.*,[41] the stress relaxation is fitted to an extended Maxwell model of the form

$$C^N(t) = A_0 e^{-(t/\tau_0)^2} \cos(\omega_0 t) + \sum_{n=1}^{N-1} A_n e^{-t/\tau_n}$$
$$+ \left(1 - \sum_{n=0}^{N-1} A_n\right) e^{-t/\tau_N}, \qquad (10)$$

where $A_0, A_1, \ldots A_{N-1}$ and $\tau_0, \tau_1, \ldots, \tau_N$ are the amplitudes and characteristic relaxation times, respectively. The first term describes the fast phonon mode and the exponential terms describe the slower structural relaxations, and we impose $\tau_1 < \cdots < \tau_N$. The first term goes to zero after short times characterizing the phonon mode, and we recover the

TABLE I. Fitting parameters for Eq. (10) for $T = 0.2$ and $T = 0.1$. The fits of Eq. (10) are carried out on the sample averaged data. Parameters are given with two significant digits.

T	A_0	A_1	A_2	A_3	τ_0	τ_1	τ_2	τ_3
0.20	0.22	0.70	0.08	0.0055	0.39	0.36	3.0	38
0.10	0.64	0.22	0.12	0.017	0.066	1.5	19	129

multicomponent Maxwell model[42] $C^N(t) = \sum_{n=1}^{N} A_n e^{-t/\tau_n}$, where $A_N = 1 - \sum_{n=0}^{N-1} A_n$ from above. The oscillatory phonon mode is roughly temperature independent in the temperature regime we study here, and in the fitting protocol, we therefore fix $\omega_0 = 8$ for $T > 0.1$. For $T \leq 0.1$, the oscillations are suppressed and the cosine trigonometric factor is set to unity to avoid over-parametrization. From the best fit, we are able to resolve four characteristic relaxation times τ_0, τ_1, τ_2, and τ_3; see Table I for temperatures $T = 0.2$ and 0.1. The system likely features more relaxation times, though these cannot be resolved from the data available. The fits of Eq. (10) to data are also plotted in Fig. 3. In general, the relaxation times increase as the temperature decreases and the amplitudes increase for the slow modes (τ_2 and τ_3) as the temperature decreases, which is also expected. For example, at $T = 0.2$, $\tau_3 \approx 40$, and at $T = 0.1$, $\tau_3 \approx 130$. However, large uncertainties in the fitted parameter values prevent us from drawing any quantitative conclusions from these parameters beyond overall trends. A deeper understanding of the parameter space and model uncertainties can be gained through Monte Carlo type analysis;[43] however, this is beyond the current scope. It is worth noting that using a large spectrum of fixed characteristic times and fitting the corresponding amplitudes as performed in Ref. 40 for data over a wider range of time scales yield poor agreement between Eq. (10) and simulation data.

In frequency space, we have $G^*(\omega)/i\omega = \eta^*(\omega) \propto C^N(\omega)$, where $C^N(\omega)$ is the normalized Fourier-Laplace transformed stress relaxation function; hence to investigate the frequency-dependent mechanical properties, we start by studying the normalized stress autocorrelation function $C^N(\omega)$. For small frequencies $\omega < \omega_0$, i.e., at frequencies where the phonon mode can be ignored, the normalized stress relaxation is given by
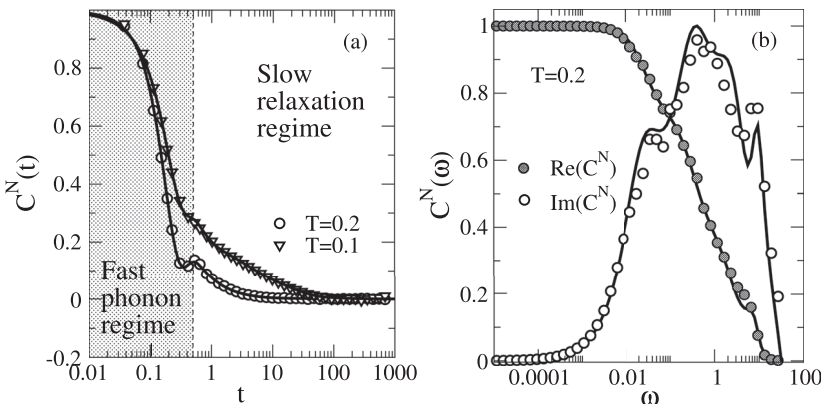

FIG. 3. (a) Normalized stress autocorrelation function for $T = 0.2$ (open circles) and $T = 0.1$ (open triangles). Lines are best fit to Eq. (10). (b) Corresponding spectrum for $T = 0.2$. The statistical uncertainties are given by the symbol size.

$$C^N(\omega) \approx \sum_{n=1}^{N} \frac{A_n/\tau_n}{1/\tau_n^2 + \omega^2} + i \sum_{n=1}^{N} \frac{A_n\omega}{1/\tau_n^2 + \omega^2}. \quad (11)$$

Hence in the small frequency regime $\omega \ll 1/\tau_N$, the stress autocorrelation function is real and $C^N \approx \sum_n A_n \tau_n$, which characterizes the purely viscous behavior or, equivalently, a large loss modulus. In the frequency range $\omega_0 > \omega > 1/\tau_n$, $n = 1, 2, 3$, we have $C^N(\omega) \approx i\sum_n A_n/\omega$, which characterizes the elastic regime, or a large storage modulus. The different relaxation times and dynamical regimes can be observed in Fig. 3(b), where the four characteristic time scales can clearly be seen as distinct peaks in the imaginary part of the spectrum. Note that here the lines are Fourier-Laplace transforms of the fit to Eq. (10) and symbols represent the Fourier-Laplace transform of the data. At low frequencies, the model features purely viscous behavior. Growth in the imaginary part of C^N indicates increasing and predominantly elastic response.

The mechanical properties are often discussed in terms of the magnitude of the dynamic modulus, $|G^*|$, and phase angle, δ. We plot these two quantities as functions of frequency in Fig. 4(a). Both the transformations of the data (symbols) and fit (lines) are shown. Again, the viscous regime is visible for $\omega < 10^{-2}$, where $|G^*| \propto \omega$ and $\delta \to \pi/2$. For larger frequencies, the model behaves viscoelastically, which is particularly evident from the phase angle. Several empirical models for the magnitude of the dynamic modulus and the phase shift have been proposed. For example, the Christensen-Anderson model (CA model) for the modulus and phase angle reads[44,45]

$$|G^*|(\omega) = G_g \left(1 + \left[\frac{\omega}{\omega_c}\right]^{-\nu}\right)^{-1/\nu} \text{ and } \delta(\omega) = \frac{\pi}{2}\left(1 + \left[\frac{\omega}{\omega_c}\right]^{\nu}\right)^{-1}, \quad (12)$$

where $\nu = \ln(2)/R$, R being the so-called rheological index, and ω_c is the frequency crossover. The CA model is shown in Fig. 4(a) using $\omega_c = 0.032$, $\nu = 0.9$, and $G_g = 0.9$. The glassy modulus G_g was chosen as a scaling factor. The ω_c parameter was varied in the fit rather than being set to the frequency at unit phase angle tangent in order to improve the fit at lower frequencies. Clearly, this simple model fails to predict the rich high-end frequency features of the model mechanics. However, the fit can be used to extract characteristic time and pressure scales. da Silva *et al.*[45] found that $\omega_c \approx 10^4$ s^{-1} and $G_g \approx 0.1$ GPa for two bitumens extracted from different sources. This gives a characteristic time scale

for the model of approximately 3 μs and a characteristic pressure scale of approximately 0.1 GPa. This means that for the temperatures studied here we get viscosities in the interval $4000 < \eta_0 < 25\,600$ Pa·s which is in the interval of real bitumens. Note that the glassy modulus, G_g, and the characteristic frequency, ω_c, can vary considerably depending on the crude oil source.[40]

In bitumen experiments, the accessible frequency range is often limited to 10^{-2}–10^2 Hz.[46] In order to study the mechanical properties in the high-frequency limit, time-temperature superposition (TTS) is often applied.[42] The basic assumption of TTS is that the same physical processes are present at all temperatures, but they take place on a different time scale as the processes are affected by the temperature. Figure 4(b) shows $|G^*|$ scaled by the factor $b_T = T/T_{ref}$ versus frequency scaled by the factor $a_T = \eta_0(T)/\eta_0(T_{ref})$.[47] It is observed that TTS is obeyed in the viscous regime but fails in the high-frequency viscoelastic regime, especially at the lowest temperature. Thus, we conjecture that different processes take place at higher frequencies and at different temperatures.

Lemarchand *et al.*[4] performed detailed molecular dynamics simulations of the Cooee-bitumen model[14] mentioned above, and it was shown that the slow rotation of the asphaltene aggregates correlates with viscosity. To see if the present model also features this correlation, the stress relaxation times, $\tau_0, \ldots, \tau_3$, were compared to the relaxation times for two different single particle processes. To this end, we define the normalized rotational correlation function for the cyclo-butamer as $C_{rot}(t) = \langle \mathbf{n}(t)\cdot\mathbf{n}(0)\rangle$,[37] where $\mathbf{n}(t)$ is the unit vector normal to the plane spanned by two of the bonds in the molecule. Likewise, the end-to-end correlation function for the pentamer is found from $C_{ee}(t) = \langle \mathbf{u}(t)\cdot\mathbf{u}(0)\rangle$, where $\mathbf{u}$ is the vector of separation between the first and last DPD-particle in the pentamer. C_{rot} and C_{ee} are plotted as functions of time in Fig. 5. These single-particle relaxation processes follow a single exponential decay with relaxation times that are much larger than the characteristic relaxation times for the stress. For example, $\tau_3 \approx 30$ which is much smaller than both τ_{rot} and τ_{ee}. Also, in this model, the rotational relaxation is faster than the end-to-end relaxation, which further indicates that the slow modes in the stress relaxation are not dominated by single-particle rotation. Finally, the single-particle properties studied here are not affected significantly by the composition, whereas the stress relaxation is. This indicates that the stress relaxation is not dominated by a single-particle process but instead is a
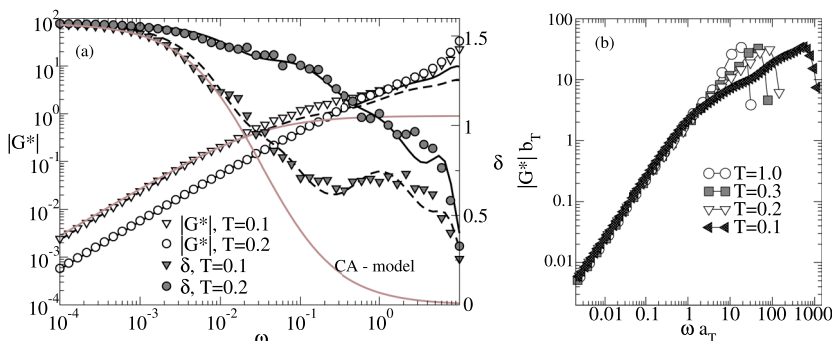

FIG. 4. (a) The magnitude of the dynamic modulus, $|G^*|$, and phase angle, δ, for ROSE model bitumen. Full lines are fits of Eq. (12); parameters are listed in the text. (b) Time-temperature-superposition (TTS) plot. $a_T = \eta_0(T)/\eta_0(T_{ref})$ and $b_T = T_{ref}/T$, where $T_{ref} = 1.0$ is used.
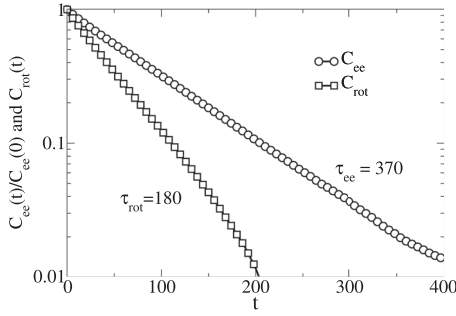
FIG. 5. The cyclo-butamer rotational and pentamer end-to-end autocorrelation functions. $T = 0.2$.

B. Dynamical properties

Figure 6 shows the normalized longitudinal velocity autocorrelation function, C_{uu}^N, and density autocorrelation function, $C_{\rho\rho}^N$, for the two smallest wavevectors accessible in our system at $T = 0.2$. We fit the hydrodynamic predictions to the data using[35,37]

$$C_{uu}^N(k,t) \approx e^{-\Gamma k^2 t} \cos(kc_s t) \qquad (13)$$

and

$$C_{\rho\rho}^N(k,t) = K e^{-D_T k^2 t} + (1-K) e^{-\Gamma k^2 t} \cos(kc_s t), \qquad (14)$$

where Γ is the sound attenuation coefficient, c_s is the adiabatic speed of sound, D_T is the thermal diffusion coefficient, and K is a weight factor. The fitting protocol was the following: (i) Eq. (13) is fitted to the longitudinal velocity autocorrelation function data for $k = 0.74$ and $k = 1.49$. From this, we obtain values for the sound attenuation coefficient Γ and the speed of sound c_s. These values are then used to fit Eq. (14) to the density autocorrelation function data using the diffusion coefficient D_T and weight factor K as free fitting parameters. Table II lists the results. It is worth pointing out that while Eq. (13) fits data very well, the agreement of Eq. (14) with the data is less satisfactory especially at small times, which indicates that D_T is time dependent. Also, from the table, we see that the hydrodynamic coefficients D_T, Γ, and c_s depend on the wavevector, meaning that the values in Table II are not the zero-wavevector values.

Returning to Fig. 6(b), we observe that the density autocorrelation has two different dynamical regimes. At first, there is a fast dampened oscillatory regime, which is a fingerprint of
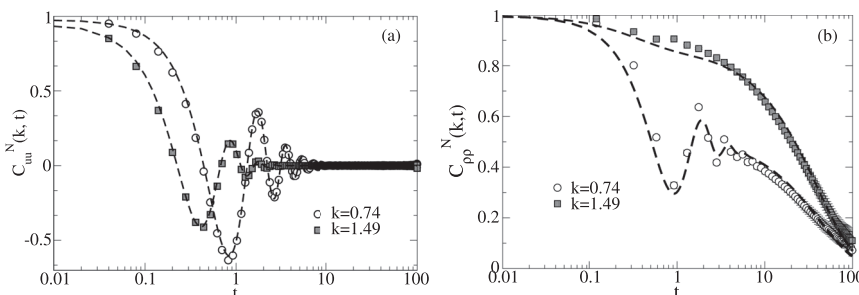
TABLE II. Hydrodynamic coefficients for the bitumen model at $T = 0.2$.

k	D_T	Γ	c_s	K
0.74	0.044 ± 0.005	1.04 ± 0.01	4.79 ± 0.00	0.52 ± 0.0
1.49	0.012 ± 0.001	0.93 ± 0.00	4.69 ± 0.00	0.88 ± 0.01

propagating density waves. After this, a slow decaying exponential regime is observed due to the thermal diffusion process. This is also evident from the coefficients D_T and Γ in Table II. Since these two processes have such different characteristic time scales, the two processes are completely decoupled on large length scales.

The corresponding dynamic structure factor is found by a Fourier transform of the data. However, as the simulation data do not converge to zero in the sampling time span, a direct numerical transformation is not possible. Furthermore, an exponential extrapolation of the data is associated with large uncertainties and is also not applicable. Therefore we discuss the dynamic structure factor qualitatively in the following. From D_T and Γ, we can infer that the dynamic structure factor for the model is characterized by a sharp Rayleigh peak (due to the thermal process) and a relatively broad Brillouin peak (the density wave propagation), at least for low wavevectors. This can also be stated in terms of the Landau-Placzek ratio,[48] which is the ratio of the Rayleigh and Brillouin integral regions; for the model, this ratio is approximately unity. Naturally, it would be interesting to compare the dynamic structure factor to experimental data, but to our knowledge, no such dynamical study on bitumen exists in the literature.

C. Polymer-modified bitumen mixtures

The mechanical properties of the unmodified model bitumen serve as reference for the effects of adding a triblock copolymer. In Fig. 7(a), the stress relaxation is plotted for three different polymer concentrations where $a_{BS} = a_{BB} = a_{SS} = 25$, i.e., a homopolymer of 20 identical units. The corresponding mass fractions are from approximately 1% to 10%. The broken lines represent the best fit of Eq. (10) using $N = 4$; that is, five characteristic times scales can be resolved, $\tau_0, \ldots, \tau_4$. The characteristic time scales are all affected by the addition of polymers. For example, for $N_{\text{pol}} = 10$ at $T = 0.2$, we get $\tau_0 = 0.022$, $\tau_1 = 2.3$, $\tau_2 = 19$, $\tau_3 = 100$, and $\tau_4 = 600$. The inset shows the corresponding spectrum for a polymer concentration of 5.2% ($N_{\text{pol}} = 6$). It is clearly seen that an additional slow mode, which is not present in pure bitumen,

FIG. 6. (a) The longitudinal velocity autocorrelation function. (b) The density autocorrelation function. In both [(a) and (b)], symbols represent data and broken lines represent best fits to Eqs. (13) and (14), respectively. $T = 0.2$.
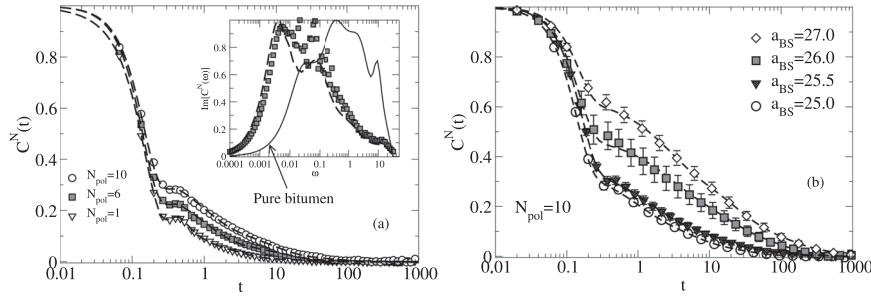
FIG. 7. (a) Normalized stress autocorrelation for different polymer concentrations at $a_{BS} = 25$ and $T = 0.2$. The broken lines are best fits of Eq. (10) to data using $N = 4$. The inset shows the imaginary part of the corresponding spectrum for $N_{pol} = 6$. Also, the spectrum for pure bitumen at $T = 0.2$ is shown as a full line for comparison. The statistical uncertainties are of the size of the symbols. (b) Normalized stress autocorrelation for different repulsion parameters and mass fractions of 8.3% ($N_{pol} = 10$) and $T = 0.2$.

has emerged around $\omega \sim 0.01$. Figure 7(b) shows the stress relaxation for increasing B-S repulsion parameters while keeping the polymer concentration fixed. The relaxation is dramatically affected and features a very slow decay, i.e., the viscosity increases significantly. It is also worth noting that the statistical uncertainties are relatively large for repulsion parameters $a_{BS} = 26$ and 27, indicating that the system undergoes transitions where it is trapped in different microscopic configurations with very different internal stresses. This is especially pronounced for $a_{BS} = 26$.

The viscosity for polymer-modified bitumen is calculated as for the unmodified bitumen. For systems with high polymer concentrations, this viscosity is estimated from an integration of the fitting function, Eq. (10), rather than directly calculated, because the stress relaxation function has not fully decayed in the time window imposed for averaging at the start of the simulation. Using this method, we are only able to estimate a lower limit of the viscosity for the high concentrations and not any error estimates. Table III summarizes the results for selected mixtures.

To get information about the polymer chain conformations, the average intra-polymer squared end-to-end distance is calculated. This is defined by $\langle R_e^2 \rangle = \langle \sum_{i=1}^{N_{pol}} (\mathbf{r}_{i\alpha} - \mathbf{r}_{i\beta})^2 \rangle / N_{pol}$, where $i\alpha$ and $i\beta$ are the end DPD particles in polymer chain i. The results are listed in Table III. Within statistical uncertainty, the end-to-end distance is unaffected by the polymer concentration and follows the results from the random walk of freely rotating polymers[49] with $\langle R_e^2 \rangle = (N_{pol} - 1) l_b^2 \approx 19$ (based on an average bond length of one). As the repulsion parameter increases, the polymer backbone conformation also changes and the end monoblock distances decrease significantly. The

former effect is associated with a contrasting increase in the radius of gyration, defined as $R_g = \langle \sum_{i=1}^{N_{pol}} \sum_{\alpha} (\mathbf{r}_{i\alpha} - \mathbf{R}_i)^2 \rangle / N_{pol}$, where $\mathbf{R}_i$ is the chain i center-of-mass. This indicates swelling of the polymer without extending the chain ends. This is not so surprising as the end blocks, formed of S particles, are now energetically favored when they are closer to each other and farther from the middle block, formed of B particles. On the contrary, the middle block is energetically favored when it is closer to other B particles rather than to the S particles of the end blocks. Also, note here that for unperturbed freely rotating polymers following a random walk, these lengths are related as $\langle R_g^2 \rangle = \langle R_e^2 \rangle / 6$;[49] the model follows this approximately within statistical uncertainty for repulsion parameter $a_{BS} = 25$, corresponding to the homopolymer case. The inter-polymer end-to-end distance quantifies the distance between ends of separate chains; we define it as

$$\langle R_e^2 \rangle_{\text{inter}} = \frac{1}{4N_{\text{pair}}} \left\langle \sum_i^{N_{pol}-1} \sum_{j>i}^{N_{pol}} (\mathbf{r}_{i\alpha} - \mathbf{r}_{j\alpha})^2 + (\mathbf{r}_{i\alpha} - \mathbf{r}_{j\beta})^2 \right.$$
$$\left. + (\mathbf{r}_{i\beta} - \mathbf{r}_{j\alpha})^2 + (\mathbf{r}_{i\beta} - \mathbf{r}_{j\beta})^2 \right\rangle, \tag{15}$$

where N_{pair} denotes the number of polymer pairs. $\langle R_e^2 \rangle_{\text{inter}}$ shows that for larger repulsion, the average distance between end-group blocks of separate chains decreases, indicating that these end-group blocks form clusters in the bitumen. These clusters are stable at the highest repulsion simulated, while for intermediate repulsion, they vary in size and number. Two different snapshots of the polymers in a simulation with $a_{BS} = 27$ are shown in Fig. 8. In Fig. 8(a), three smaller

TABLE III. Estimated viscosities, inter- and intra-polymer end-to-end distances, and squared radii of gyration for the different model mixtures. Values with error estimates (standard deviations) are found directly from simulation data, while an asterisk indicates that the value is found from the integral of the fitting function, Eq. (10).

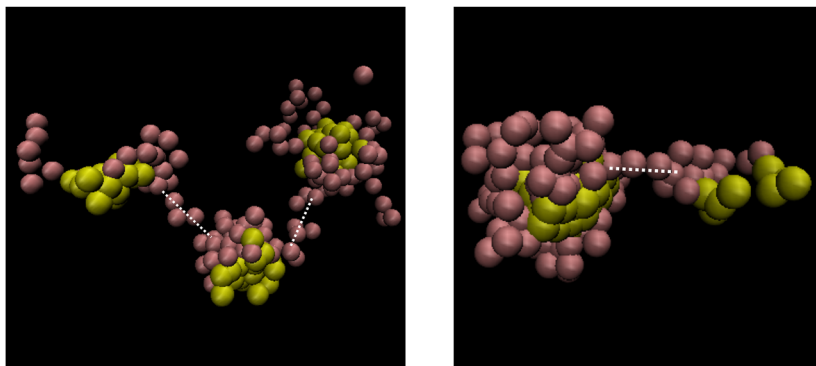| N_{pol}	0	1	4	8	10	10	10	10
Mass fraction (%)	0	0.9	3.5	6.8	8.3	8.3	8.3	8.3
a_{BS}	...	25	25	25	25	25.5	26	27
η_0	13 ± 2	19 ± 2	65^*	160^*	190^*	380^*	$>10^{3*}$	$>10^{3*}$
$\langle R_e^2 \rangle$	...	18 ± 6	10 ± 4	15 ± 2	13 ± 2	16 ± 3	4.2 ± 0.3	4.1 ± 0.7
$\langle R_g^2 \rangle$	...	3.7 ± 0.9	2.8 ± 0.4	3.8 ± 0.8	3.2 ± 0.2	2.8 ± 0.5	4.8 ± 0.8	4.4 ± 0.2
$\langle R_e^2 \rangle_{\text{inter}}$	...	...	...	...	18.8 ± 0.3	17.6 ± 0.5	7.1 ± 0.5	4.1 ± 0.6

FIG. 8. Snapshot of the polymer bead position for $a_{BS} = 27$ showing a polymer network. Yellow spheres represent S particles, and brown spheres represent B particles. The white dashed lines represent the bridges forming the polymer network.

clusters of mono-blocks are identified (yellow spheres represent S particles, and brown spheres represent B particles). Importantly, the clusters are interconnected by the polymer backbone forming a polymer network. In Fig. 8(b), on the other hand, only two clusters are interconnected. It is important to stress that this is not a matter of equilibration (within the duration of the simulations) as the transitions between the different configurations occur continuously. We conjecture that it is these different microscopic configurations that lead to the increased noise in the stress relaxation curves seen in Fig. 7.

The formation of end-group block clusters and polymer networks means that polymer rearrangements happen as a large scale collective re-arrangement characterized by a slow relaxation time. This slow collective motion governs the stress relaxation and thus the increasing viscosity.

Because of the simplicity of the model, the formation of small monoblock clusters can be analyzed in a framework similar to the lattice-based Flory-Huggins theory.[28] To this end, we consider the system in terms of the single DPD-particle, B and S, and write the Helmholtz free energy, F, as a function of the B-particle concentration, $x = \rho_B/\rho$,

$$\frac{F}{k_B T} = x \ln(x) + (1 - x) \ln(1 - x) + \chi(1 - x)x. \quad (16)$$

One can show for monomers of B and S that for $\chi > \chi^{\mathrm{crit}} = 2$, the free energy features two minima allowing for segregation. Groot and Warren argued[28] that the χ-parameter for DPD

particles can be approximated using the relation

$$\chi = \frac{2\alpha(a_{BS} - a_{BB})(\rho_B + \rho_S)}{k_B T}, \quad (17)$$

where α is a second virial coefficient found from the equation of state

$$\frac{p - \rho k_B T}{a_{BB}} = \alpha \rho^2, \quad (18)$$

where p is the pressure, $p = -\mathrm{trace}(\sigma)/3$. Simulation results[22] show that the model follows the equation of state [Eq. (18)] with $\alpha = 0.10 \pm 0.03$ in the density range from 2.2–4.7 and is independent of the presence of polymers. It is important to note that this value of α is also found in the original work of Groot and Warren treating a simple DPD-system. At the state point $T = 0.2$ and $\rho = 4.0$, the χ-parameter is $\chi \approx 4(a_{BS} - a_{BB})$; hence, the simplest Flory-Huggins theory predicts segregation for $a_{BS} > 25.5$.

As a final result, we plot the magnitude of the dynamic modulus and the phase angle of different model polymer modified bitumens in Fig. 9. Changing the polymer concentration only has a small effect on the mechanical properties; however, changing the interaction parameter by a few percent significantly changes both the shear resistance and elastic response.

IV. CONCLUSION

We have presented a simple mesoscopic model for bitumen and bituminous mixtures. The model features the expected mechanical behavior for sufficiently low temperatures: Addition of polymers increases the viscosity and shifts the viscoelastic regime toward lower frequencies. The viscosity depends on the polymer concentration in agreement with experimental observations. The mechanical properties are also affected by changing interactions between the end-block and bitumen, which can induce phase separation and microstructure. The underlying mechanism behind this lies in the formation of end-block clusters. For sufficiently large repulsion, these clusters are stable and segregate in the mixture. For intermediate repulsion, the cluster sizes are small and dynamical and are connected by the polymer backbone mono-block.

The model demonstrates the need for a polymer-modified bitumen to exhibit a supra-molecular microphase separation
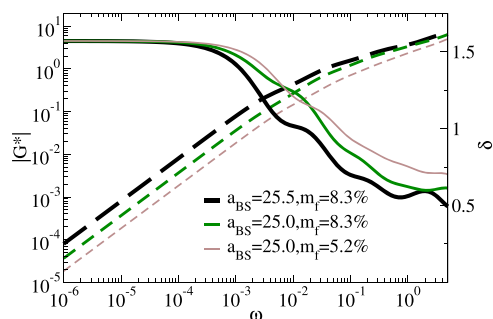

FIG. 9. The magnitude of the dynamic modulus $|G^*|$ (dashed line) and phase angle δ (solid line) for different polymer modified bitumens, calculated using the fits of Eq. (10) to averaged data.

in order to be effective. It becomes a bitumen–polymer composite, and this inhomogeneous material provides the changes in mechanical response. Returning to the $|G^*|/\sin(\delta)$ specification, the results show how addition of polymers increases the rutting resistance for all frequencies. Especially at low frequencies, the rutting resistance improvement is due to the increased viscosity induced by microstructure in the polymer-modified bitumen.

The model is not unique in the sense that the choice of molecules (or dynamic entities) can be varied, but the resulting systems will likely show similar mechanics. As indicated by the Flory-Huggins treatment, the phase separation of the triblock copolymer is independent of the molecular model for the bitumen. However, the effect of the bitumen model on the mechanical properties of the bitumen mixture is not clear from the current analysis. Also, the choice of parameters and molecule relative concentrations can be tuned in order to mimic specific bituminous systems. The model is coarse grained, which allows for a qualitative study of the mechanical properties of bituminous mixtures over sufficiently large length scales and long time scales. This can allow further effects on mechanical properties of polymer bond stiffness, polymer size, effects of branching, and more to be investigated.

ACKNOWLEDGMENTS

[1]J. F. Branthaver, J. C. Petersen, R. E. Robertson, J. J. Duvall, S. S. Kim, P. M. Harnsberger, T. Mill, E. K. Ensley, F. A. Barbour, and J. F. Schabron, "Binder characterizationand evaluation volume 2: Chemistry," Technical Report No. SRHP-A-368, Natural Research Council, 1993.

[2]I. A. Wiehe and K. S. Liang, "Asphaltenes, resins, and other petroleum macromolecules," Fluid Phase Equilib. **117**, 201 (1996).

[3]ASTM D4124-09, "Standard test method for separation of asphalt into four fractions," Technical Report No. ASTM D4124-09, Natural Research Council, 2009.

[4]C. A. Lemarchand, T. B. Schrøder, J. C. Dyre, and J. S. Hansen, "Cooee bitumen: Chemical aging," J. Chem. Phys. **139**, 124506 (2013).

[5]J. Zhu, B. Birgisson, and N. Kringos, "Polymer modification of bitumen: Advances and challenges," Eur. Polym. J. **54**, 18 (2014).

[6]L. Zhang and L. Greenfield, "Molecular orientation in model asphalt using molecular simulation," Energy Fuels **21**, 1102–1111 (2007).

[7]L. Zhang and M. L. Greenfield, "Relaxation time, diffusion and viscosity analysis of model asphalt systems using molecular simulation," J. Chem. Phys. **127**, 194502 (2007).

[8]L. Zhang and L. Greenfield, "Rotational relaxation times of individual compounds within simulations of molecular asphalt models," J. Chem. Phys. **132**, 184502 (2010).

[9]C. A. Lemarchand, T. B. Schrøder, J. C. Dyre, and J. S. Hansen, "Cooee bitumen. II. Stability of linear asphaltene nanoaggregates," J. Chem. Phys. **141**, 144308 (2014).

[10]C. A. Lemarchand, M. L. Greenfield, and J. S. Hansen, "Dynamics and structure of Bitumen-water mixtures," J. Phys. Chem. B **120**, 5470 (2015).

[11]D. D. Li and M. L. Greenfield, "Chemical compositions of improved model asphalt systems for molecular simulations," Fuel **115**, 347–356 (2014).

[12]D. D. Li and M. L. Greenfield, "Viscosity, relaxation time, and dynamics within a model asphalt of larger molecules," J. Chem. Phys. **140**, 034507 (2014).

[13]L. Zhang and L. Greenfield, "Analyzing properties of model asphalt using molecular simulation," Energy Fuels **21**, 1712–1716 (2007).

[14]J. S. Hansen, C. A. Lemarchand, E. Nielsen, J. C. Dyre, and T. B. Schrøder, "Four-component united-atom model of bitumen," J. Chem. Phys. **138**, 094508 (2013).

[15]N. P. Bailey, T. S. Ingebrigtsen, J. S. Hansen, A. A. Veldhorst, L. Bøhling, C. A. Lemarchand, A. E. Olsen, A. K. Bacher, L. Costigliola, U. R. Pedersen, H. Larsen, J. C. Dyre, and T. B. Schrøder, "RUMD: A general purpose molecular dynamics package optimized to utilize GPU hardware down to a few thousand particle," SciPost Phys. **3**, 038 (2017).

[16]F. Khabaz and R. Khare, "Glass transition and molecular mobility in styrene-butadiene rubber modified asphalt," J. Phys. Chem. B **119**, 14261–14269 (2015).

[17]M. Masoori and M. L. Greenfield, "Frequency analysis of model asphalt molecular dynamics," J. Chem. Phys. **141**, 124504 (2014).

[18]M. Masoori and M. L. Greenfield, "Reducing noise in computed correlation functions using techniques from signal processing," Mol. Simul. **43**, 1485–1495 (2017).

[19]C. A. Lemarchand, N. P. Bailey, B. D. Todd, P. J. Daivis, and J. S. Hansen, "Non-Newtonian behavior and molecular structure of Cooee bitumen under shear flow: A non-equilibrium molecular dynamics study," J. Chem. Phys. **142**(24), 244501 (2015).

[20]L. Zhang and L. Greenfield, "Effect of polymer modification in properties and microstructures of model asphalt systems," Energy Fuels **22**, 3363–3375 (2007).

[21]F. Khabaz and R. Khare, "Molecular simulations of asphalt rheology: Application of time–temperature superposition principle," J. Rheol. **62**, 941–954 (2018).

[22]M. L. Greenfield, C. A. Lemarchand, and J. S. Hansen, "Mechanics induced by simple shapes within dissipative particle dynamics simulations," Phys. Chem. Chem. Phys. (unpublished).

[23]T. W. Kennedy, G. A. Huber, E. T. Harrigan, R. J. Cominsky, C. S. Hughes, H. Von Quintus, and J. S. Moulthrop, "Superior performing asphalt pavements (Superpave): The product of the SHRP asphalt research program," Technical Report No. SHRP-A-410, Strategic Highway Research Program, 1994, Available on-line from http://www.trb.org/publications/shrp/SHRP-A-410.pdf.

[24]G. D. Airey, "Rheological properties of styrene butadiene styrene polymer modified road bitumens," Fuel **82**, 1709–1719 (2003).

[25]J. F. Masson, P. Collins, G. Robertson, J. R. Woods, and J. Margeson, "Thermodynamics, phase diagrams, and stability of bitumen–polymer blends," Energy Fuels **17**, 714–724 (2003).

[26]P. J. Hoogerbrugge and J. M. V. A. Koelman, "Simulating microscopic hydrodynamics phenomena with dissipative particle dynamics," Europhys. Lett. **19**, 155 (1992).

[27]P. Español and P. Warren, "Statistical mechanics of dissipative particle dynamics," Europhys. Lett. **30**, 191 (1995).

[28]R. D. Groot and P. B. Warren, "Dissipative particle dynamics: Bridging the gap between atomistic and mesoscopic simulation," J. Chem. Phys. **107**, 4423 (1997).

[29]M. P. Allen and D. J. Tildesley, *Computer Simulation of Liquids* (Clarendon Press, New York, 1989).

[30]J. S. Hansen, https://github.com/jesperschmidthansen/seplib.

[31]J. H. Irving and J. G. Kirkwood, "The statistical mechanical theory of transport processes. IV. The equations of hydrodynamics," J. Chem. Phys. **18**, 817–829 (1950).

[32]P. Español and F. Vázquez, "Coarse-graining from coarse-grained descriptions," Philos. Trans. R. Soc., A **360**, 383 (2002).

[33]M. H. Ernst and R. Brito, "New Green-Kubo formulas for transport coefficients in hard-sphere, Langevin fluids and the likes," Europhys. Lett. **73**, 183 (2006).

[34]G. Jung and F. Schmid, "Computing bulk and shear viscosities from simulations of fluids with dissipative and stochastic interactions," J. Chem. Phys. **144**, 204104 (2016).

[35]J. S. Hansen, M. L. Greenfield, and J. C. Dyre, "Hydrodynamic relaxations in dissipative particle dynamics," J. Chem. Phys. **148**, 034503 (2018).

[36]B. D. Todd and P. J. Daivis, "Homogeneous non-equilibrium molecular dynamics simulations of viscous flow: Techniques and applications," Mol. Simul. **33**(3), 189–229 (2007).

[37]J. P. Hansen and I. R. McDonald, *Theory of Simple Liquids* (Academic Press, Amsterdam, 2006).

[38]T. D. Khong, S. L. Malhotra, and L.-P. Blanchard, "Rheological behaviour of asphalts," Rheol. Acta **18**, 382–391 (1979).

[39]H. Zhai and D. Salomon, "Evaluation of low-temperature properties and the fragility of asphalt binders with non-Arrhenius viscosity-temperature dependence," Transp. Res. Rec. **1901**, 44–51 (2005).

[40]J. V. Badami and M. L. Greenfield, "Maxwell model analysis of bitumen rheological data," J. Mater. Civ. Eng. **23**, 1387 (2011).

[41]R. Hartkamp, P. J. Daivis, and B. D. Todd, "Density dependence of the stress relaxation function of a simple liquid," Phys. Rev. E **87**, 032155 (2013).

[42]J. D. Ferry, *Viscoelastic Properties of Polymers* (Wiley & Sons, Inc., New York, 1980).

[43]K. S. Brown and J. P. Sethna, "Statistical mechanical approaches to models with many poorly known parameters," Phys. Rev. E **68**, 021904 (2003).

[44]D. W. Christensen, Jr. and D. A. Anderson, "Interpretation of dynamic mechanical test data for paving grade asphalt cements," J. Assoc. Asphalt Paving Technol. **61**, 67 (1992).

[45]L. S. da Silva, M. M. C. Forte, L. A. Vignol, and N. S. M. Cardozo, "Study of rheological properties of pure and polymer-modified brazilian asphalt binders," J. Mater. Sci. **39**, 539 (2004).

[46]M. O. Marasteanu, T. Clyne, J. McGraw, X. Li, and R. Velasquez, "High-temperature rheological properties of asphalt binders," Transp. Res. Rec. **1901**, 52–59 (2005).

[47]R. B. Bird, R. C. Armstrong, and O. Hassager, *Dynamics of Polymeric Liquids* (John Wiley & Sons, 1987).

[48]H. Z. Cummins and Z. Herman, "Rayleigh and Brillouin scattering in liquids: The Landau–Placzek ratio," J. Chem. Phys. **44**, 2785 (1966).

[49]M. Doi and S. F. Edwards, *The Theory of Polymer Dynamics* (Oxford Science Publications, 1986).